

Supporting Information

High Capacity Garnet-Based All-Solid-State Lithium Batteries: Fabrication and 3D-Microstructure Resolved Modeling

*Martin Finsterbusch^{*a,b}, Timo Danner^{*c,d}, Chih-Long Tsai^a, Sven Uhlenbruck^{a,b}, Arnulf Latz^{c,d,e}, and
Olivier Guillon^{a,b,f}*

- a. Forschungszentrum Juelich GmbH, Wilhelm-Johnen Str., 52425 Juelich, Germany.
- b. Helmholtz Institute Muenster, Wilhelm-Johnen Str., 52425 Juelich, Germany.
- c. German Aerospace Centre (DLR), Pfaffenwaldring, 70569 Stuttgart, Germany.
- d. Helmholtz-Institute Ulm, Helmholtz-Str., 89081 Ulm, Germany.
- e. Institute of Electrochemistry, University of Ulm, Albert-Einstein-Allee, 89069 Ulm, Germany.
- f. Jülich-Aachen Research Alliance: JARA-Energy, 52425 Juelich, Germany.

* corresponding authors: m.finsterbusch@fz-juelich.de and timo.danner@dlr.de

Keywords: all-solid-state, ceramic, Li battery, microstructure, modeling, continuum

Experimental

1.1 X-ray powder diffraction

Secondary phase formation at the LLZ:Ta / LCO interface was investigated in addition to the DSC/TG measurements in detail using XRD. Even at 900 °C, 1000°C and 1050°C which is the sintering temperature of the mixed cathode and well above the peak at 700°C in the DSC graph, no secondary phases were visible even for dwell times of up to 2 hours, which suggests a very sluggish or self-limiting reaction.

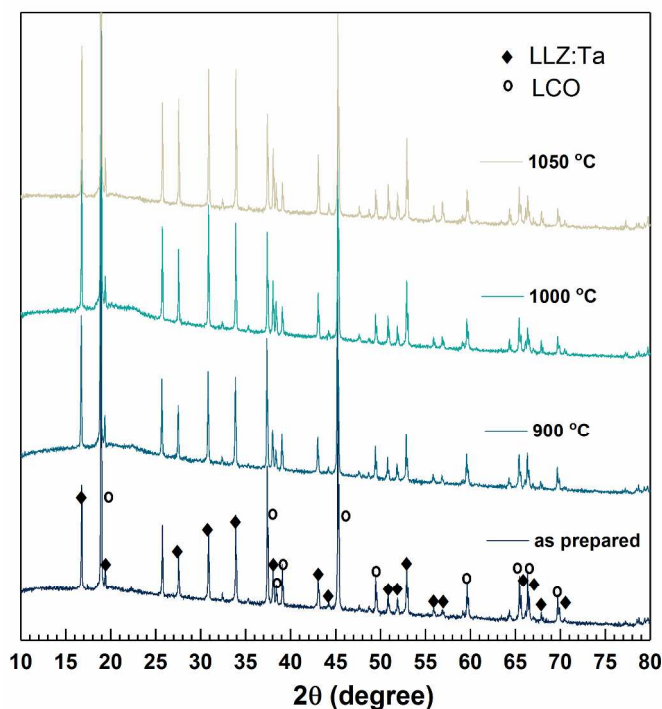


Figure S1 -X-ray diffraction (XRD) pattern of a 1:1 mixture of LLZ:Ta (solid symbols) and LCO (open symbols) and the same mixture sintered at various temperatures from 900 to 1050°C (colors).

1.2 Elemental mapping of the phase distribution

The phase distribution was verified by EDX mapping of the cross section of the sample (Figure S2), after the 3D tomography was done. It can be seen, that the LLZ:Ta (white) and LCO (grey) can be identified clearly via the La (La₁ - red) and Co (Co₁ - green) signal, and that the interface between mixed cathode and electrolyte is rather porous. No significant deviation in material composition was observed at the LLZ:Ta/LCO interface via EDX, which is not surprising since the interaction volume is much larger than the grain boundary or a possible thin secondary phase in between. A detailed study using TEM combined with e.g. EELS or EDX would be beneficial, but at this point in time was not achieved yet.

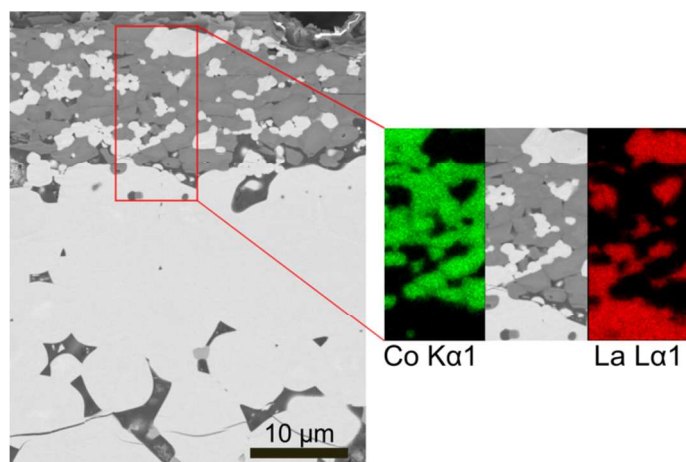


Figure S2 -Backscatter electron micrograph of a cross section of the cell with energy-dispersive X-ray spectroscopy (EDX) mapping of the Co and La distribution in the mixed cathode.

1.3 Electrochemical Impedance measurements of the full cell

To obtain the resistance values for the LCO/LLZ interface, electrochemical impedance measurements were obtained at various SOC as well as at 100°C and at 25°C. However, it was not possible to extract meaningful values from the measurements for the following reasons. First, the EIS spectra of a full cell have contributions from various interfaces, e.g. the anode current collector to the Li-metal anode, the Li/LLZ, the LLZ/LCO and the mixed cathode to cathode current collector. As can be seen from the spectra in Figure S3, only a single (depressed) semicircle is visible. Even if we assume that current collector interfaces to the electrodes remain unaltered, the Li-metal/LLZ interface will certainly change depending on temperature which was shown in previous studies for symmetric Li|LLZ|Li cells by the authors (e.g. see Ref. 15 in main manuscript) and other researcher (e.g. A. Sharafi et al.)¹. Thus, a change with temperature cannot be unambiguously assigned to the LLZ/LCO interface. Second, the EIS data shows a dependence on the state of charge for both, the 100°C and the 25°C measurements. However, trend is opposite for the two cases. At 100°C, the discharged sample shows the highest impedance; at 25°C the charged sample shows the highest impedance. This reversal can again be due to the change in the Li/LLZ interface, LLZ/ LCO interface or the change in electronic conductivity of the LCO, which is also dependent on the SOC. Even though now it appears as two semicircles are visible, this change in EIS data will convolute the issues mentioned above even further and prevents us from clearly determining the interface resistance LLZ/LCO.

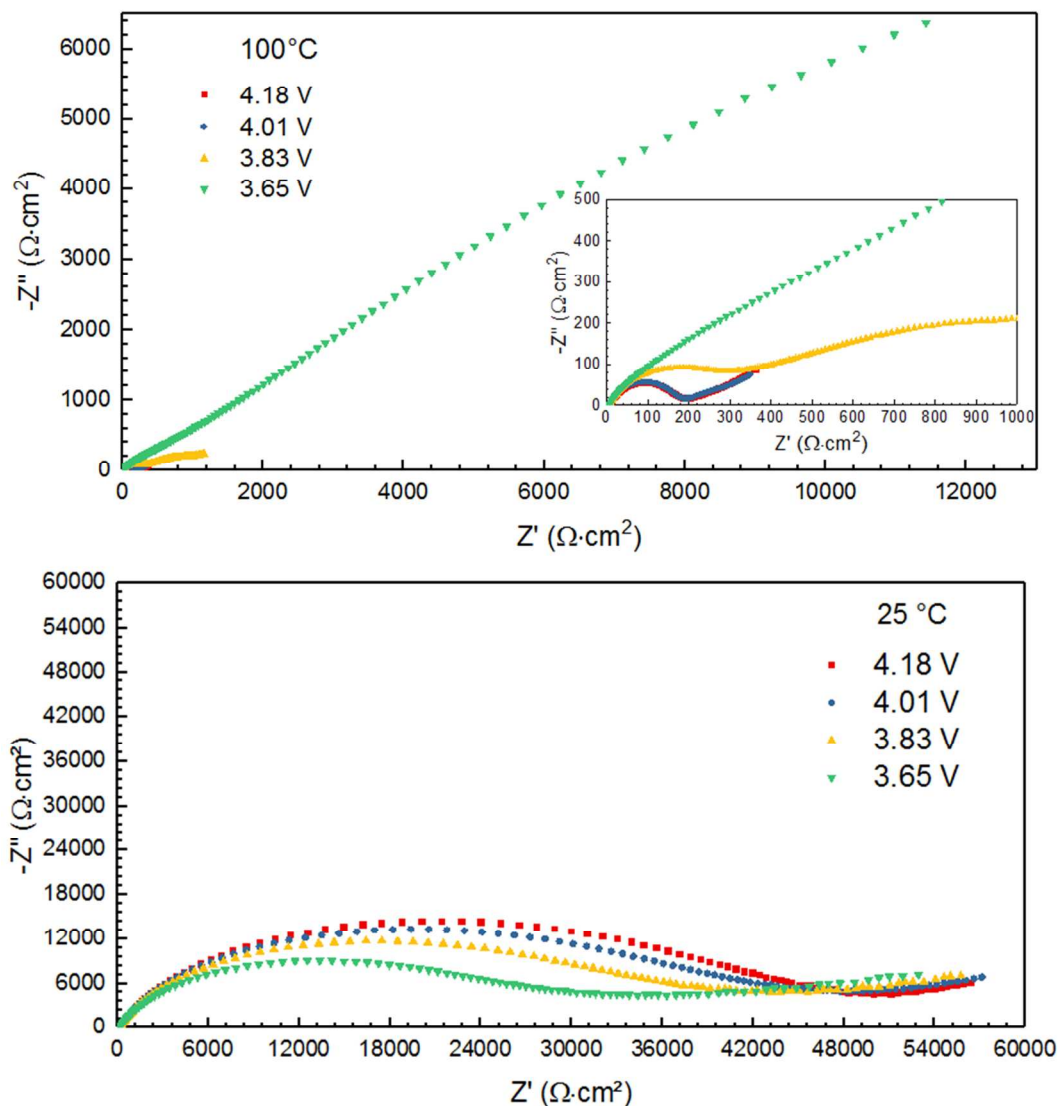


Figure S3: EIS data for a full cell at various states of charge at 100°C (top) and 25 °C (bottom)

1.3 Reconstruction data

From the 3D reconstruction, various geometric and effective parameters of the mixed LLZ/LCO cathode can be obtained. Some of these parameters, i.e. void fraction, can give direct information about possible improvements and were subsequently used to study their effect on the overall cell performance (filled w/ LLZ and filled w/ LCO cases). Other parameters, like specific surface area and relative conductivity, can be used to indirectly assess the quality of the fabricated cathode and thus give hints to improvements of the fabrication process. For example, a large anisotropic conductivity in the LLZ phase of the mixed cathode could have a negative impact on the rate capability of the cell.

The specific surface area is given as m^2 surface per m^3 electrode volume (m^{-1}). First, it is evaluated by counting the voxel surface area between the solid electrolyte and the active material. The voxel based surface area is used to estimate the true specific surface area based on a statistical approach² in the software GeoDict.

<i>Volume fractions / %</i>	
LCO	63
LLZ	30
void	7
<i>Specific surface area / m^{-1}</i>	
LCO-LLZ	$1.1 \cdot 10^6$
LCO-void	$4.9 \cdot 10^5$
LLZ-void	$3.4 \cdot 10^4$
<i>Relative conductivity $\sigma^{\text{eff}}/\sigma^0$ (x/y/z) / -</i>	
LCO	(0.45/0.40/0.42)
LLZ - reconstruction	(0.052/0.051/0.053)
LLZ – filled /w LLZ	(0.10/0.075/0.09)

Table S1 - Geometric properties and resulting effective transport parameters.

Simulation

2.1 Derivation and implementation of model equations

A detailed derivation of model equations based on the fundamental principles of non-equilibrium thermodynamics can be found in our original research articles given in the main paper. In this supplementary material we limit the discussion to a brief explanation of governing equations to provide our readers with a descriptive background of our simulation approach.

Electrode phase – A mass balance of lithium in the solid phase according to

$$\frac{\partial c_{\text{Li}}^{\text{elode}}}{\partial t} = -\nabla \cdot (-D_{\text{Li}}^{\text{elode}} \nabla c_{\text{Li}}^{\text{elode}}) \quad \text{Eq. 1}$$

is used to describe the local concentration of Li $c_{\text{Li}}^{\text{elode}}$ in the active material, where t is time and $D_{\text{Li}}^{\text{elode}}$ is the diffusion coefficient of lithium in the active material. Normalization to a maximum concentration of Li in the active material $c_{\text{Li}}^{\text{elode,max}}$ is used to define a local SOC $x = c_{\text{Li}}^{\text{elode}}/c_{\text{Li}}^{\text{elode,max}}$ for lithium in Li_xCoO_2 . The electrostatic potential in the electrode ϕ^{elode} can be calculated using the charge balance of electrons

$$0 = -\nabla \cdot i_s = -\nabla \cdot (-\sigma^{\text{elode}} \nabla \phi^{\text{elode}}), \quad \text{Eq. 2}$$

where σ^{elode} is the electronic conductivity of solid materials in the electrode. Our approach allows distinguishing between an arbitrary number of solid phases, such as active material, binder, etc. with different diffusion coefficients and conductivities which are evaluated locally as function of SOC and temperature. In the present study we model the void space as inactive solid material with negligible diffusion coefficient and conductivity.

Interface conditions - Between neighboring phases suitable boundary conditions need to be defined. In the case of LCO we assume continuity in the lithium concentration and the solid phase potential. Boundaries between LCO and void space are regarded as isolated with a zero flux condition for lithium and electrons. The interface fluxes between LLZ and LCO at the cathode are described by the well-known Butler-Volmer equation

$$i_{se} = i_{00}^{\text{LCO}} c_{\text{Li}}^{\text{elode}} \alpha^{\text{LCO}} c_{\text{Li}}^{\text{elyte}} \alpha^{\text{LCO}} (c_{\text{Li}}^{\text{elode,max}} - c_{\text{Li}}^{\text{elode}})^{(1-\alpha^{\text{LCO}})} \left[\exp\left(\frac{\alpha^{\text{LCO}} F}{RT} \eta\right) - \exp\left(-\frac{(1-\alpha^{\text{LCO}}) F}{RT} \eta\right) \right], \quad \text{Eq. 3}$$

where i_{00}^{LCO} is the exchange current density coefficient, α^{LCO} the symmetry factor of the transition state, $c_{\text{Li}}^{\text{elyte}}$ the concentration of lithium in the neighboring electrolyte, F the Faraday constant, and η the overpotential of the insertion reaction defined by

$$\eta = \phi^{\text{elode}} - \phi^{\text{elyte}} - U_0^{\text{LCO}}(x). \quad \text{Eq. 4}$$

The overpotential η can be regarded as the driving force for the insertion of lithium in the active material with the electrostatic potential of the active material ϕ^{elode} , the electrochemical potential of lithium in the electrolyte φ^{elyte} , and the open circuit potential of LCO vs. Li $U_0^{\text{LCO}}(x)$ for a specific local SOC x as defined above.

At the LLZ/Li metal interface we assume a similar expression with constant exchange current density

$$i_{se} = i_{00}^{\text{Li}} \left[\exp\left(\frac{\alpha^{\text{Li}} F}{RT} \eta\right) - \exp\left(-\frac{(1-\alpha^{\text{Li}}) F}{RT} \eta\right) \right], \quad \text{Eq. 5}$$

where the overpotential follows as

$$\eta = \phi^{\text{elode}} - \varphi^{\text{elyte}} - U_0^{\text{Li}}(x). \quad \text{Eq. 6}$$

The Butler-Volmer equation couples the current in the electrode phase to the transport in the electrolyte phase

$$n \cdot i^{\text{elode}} = n \cdot i^{\text{elyte}} = i_{se}, \quad \text{Eq. 7}$$

where the interface normal n per definition points from the electrode to the electrolyte phase. The equations for the transport in the LLZ electrolyte are described in the next paragraph.

Electrolyte phase – In our framework the material balance of Li (and vacancies) in LLZ which describes the temporal evolution of the Li concentration $c_{\text{Li}}^{\text{elyte}}$ is given by

$$\frac{\partial c_{\text{Li}}^{\text{elyte}}}{\partial t} = -\nabla \cdot \left(-D_{\text{Li}}^{\text{elyte}} \nabla c_{\text{Li}}^{\text{elyte}} + \frac{t_{\text{Li}} i^{\text{elyte}}}{F} \right), \quad \text{Eq. 8}$$

where $D_{\text{Li}}^{\text{elyte}}$ is the diffusion coefficient of Li ions in LLZ. The transference number t_{Li} defines the portion of the current in the electrolyte i^{elyte} which is transported by the Li ions and can be described by

$$i^{\text{elyte}} = -\kappa^{\text{elyte}} \nabla \varphi^{\text{elyte}} - \frac{\kappa^{\text{elyte}} (t_{\text{Li}} - 1)}{F} \frac{\partial \mu_{\text{Li}}^{\text{elyte}}}{\partial c_{\text{Li}}^{\text{elyte}}} \nabla c_{\text{Li}}^{\text{elyte}}. \quad \text{Eq. 9}$$

κ is the conductivity of LLZ and $\mu_{\text{Li}}^{\text{elyte}}$ the chemical potential of lithium ions. Based on our measurements we presume a transference number $t_{\text{Li}} = 1$. As a result Eq. 9 reduces to Ohm's law following the model proposed by Fabre *et al.* Insertion of Eq. 9 in Eq. 8 leads to

$$\frac{\partial c_{\text{Li}}^{\text{elyte}}}{\partial t} = -\nabla \cdot \left(-D_{\text{Li}}^{\text{elyte}} \nabla c_{\text{Li}}^{\text{elyte}} - \frac{\kappa^{\text{elyte}}}{F} \nabla \varphi^{\text{elyte}} \right). \quad \text{Eq. 10}$$

On the assumption of negligible interactions between Li ions and lattice vacancies we use

$$\kappa^{\text{elyte}} = D_{\text{Li}}^{\text{elyte}} \frac{c_{\text{Li}}^{\text{elyte}} F^2}{RT} \quad \text{Eq. 11}$$

as relation between electrolyte conductivity and Li diffusion coefficient and finally arrive at

$$\frac{\partial c_{\text{Li}}^{\text{elyte}}}{\partial t} = -\nabla \cdot \left(-D_{\text{Li}}^{\text{elyte}} \nabla c_{\text{Li}}^{\text{elyte}} - D_{\text{Li}}^{\text{elyte}} \frac{c_{\text{Li}}^{\text{elyte}} F}{RT} \nabla \varphi^{\text{elyte}} \right). \quad \text{Eq. 12}$$

which is similar compared to the expression based on the Nernst-Planck equation proposed by Danilov *et al.*. The resolution of electrode structures investigated in this work is between 50 and 200 nm and, therefore, about an order of magnitude larger than the thickness of space charge layers at the electrode/electrolyte interface. Following the work of Fabre *et al.* and Danilov *et al.* we, assume electro-neutrality in the solid electrolyte on this length scale. The charge balance in the electrolyte

$$0 = -\nabla \cdot i^{\text{elyte}}, \quad \text{Eq. 13}$$

provides an additional equation for the local potential in the electrolyte phase and closes our set of equations.

Computational details – The governing equations are implemented in the simulation framework CoRheoS (Complex Rheology Solver, Fraunhofer ITWM) for complex non-linear flow problems. All equations are discretized using a finite volume approach making direct use of the voxel based grid given by the tomography data. The time discretization is fully implicit and the resulting set of algebraic equations is solved with an algebraic multigrid solver (SAMG, Fraunhofer SCAI). A commercial version of the code for Li-ion batteries (BEST – Battery and Electrochemistry Simulation Tool) is available through the Fraunhofer ITWM. Simulations are performed on the JUSTUS cluster hosted by the University of Ulm and simulation time is between 1 and 4 days depending on the size of the computational domain and input parameters.

2.2 Charge simulations at elevated temperatures

In the present article we focus our discussion on the first discharge process since the cell shows a rather fast degradation, losing approx. half its capacity within the first 50 full cycles (100% DOD). In order to demonstrate the capabilities of our model we also include simulated charge curves. Comparing our simulations to the experimental data, see Fig. S4, we can deduce several conclusions. First, the capacity in the first cycle is larger compared to the expected capacity based on the scaled simulation results (dashed line). This is a strong indicator for degradation process in the first cycle. Secondly, the model is able to reproduce the cell voltage/overpotentials during Li intercalation at the pristine, non-degraded interface. Which is important for the following design studies since it provides estimates for the performance of an engineered (non-degrading) interface. Third, the model is not able to capture the overpotentials during charge for the second and all following cycles. This is another indicator for the irreversible formation of degradation products in the first cycle and an increase in the impedance of the cell. Finally, we can report good agreement between the expected (dashed line) and measured charge capacity in the second cycle. This indicates that the degradation processes in the first cycle rather occur on the electrolyte side than in the active material.

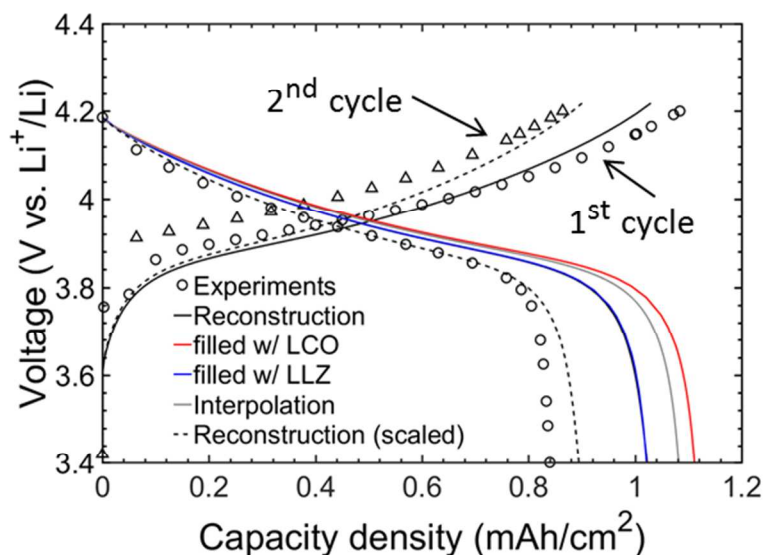


Figure S4: Measured discharge curve for the first (open circles) and second (open triangles) cycle at 100°C and simulated data for as reconstructed (black) and void-filled mixed cathode (red = LCO, grey= mixed, blue= LLZ).

2.3 Simulations at room temperature

At room temperature we observe strong deviations between our simulations and the corresponding experimental data. Since we could report favorable agreement of our simulations at 100 °C this is an indication for processes with a very high activation barrier. In order to evaluate the effect of different transport and kinetic parameters on cell performance at room temperature we performed a parameter study on the as reconstructed electrode geometry with an electrode and separator thickness of 25 μm and 500 μm , respectively. If not indicated differently the discharge current was in all cases 0.1 mA/cm^2 .

Diffusion of Li in LLZ – In our model we determined the diffusion coefficient of Li in LLZ on the assumption of negligible interactions between Li and vacancies (see Eq. 11). In order to assess the sensitivity of our simulations on this parameter we simulated additional discharge curves at 100 °C and room temperature. Results of the study are summarized in Figure S5. Solid lines indicate simulations with the as calculated diffusion coefficient and open circles correspond to simulations where the diffusion coefficient was chosen one order of magnitude smaller. Our results show that the effect of the diffusion coefficient is negligible. Closer inspection of the distribution of Li ions in the electrolyte (see Figure S5 b) reveals a quasi-homogeneous concentration throughout the battery. This result can be directly linked to our assumption of $t_{\text{Li}} = 1$. In a way we fix the anion lattice and only allow for a transport of Li ions. The postulation of electro-neutrality on the length-scale of our simulations does in the end result in vanishing concentration gradients. However, similar effects are found for (modified)

Poisson-Nernst-Planck systems if the distance to the electrified interface is sufficiently large. More detailed theories for transport and interface processes in solid electrolytes are part of our ongoing research.

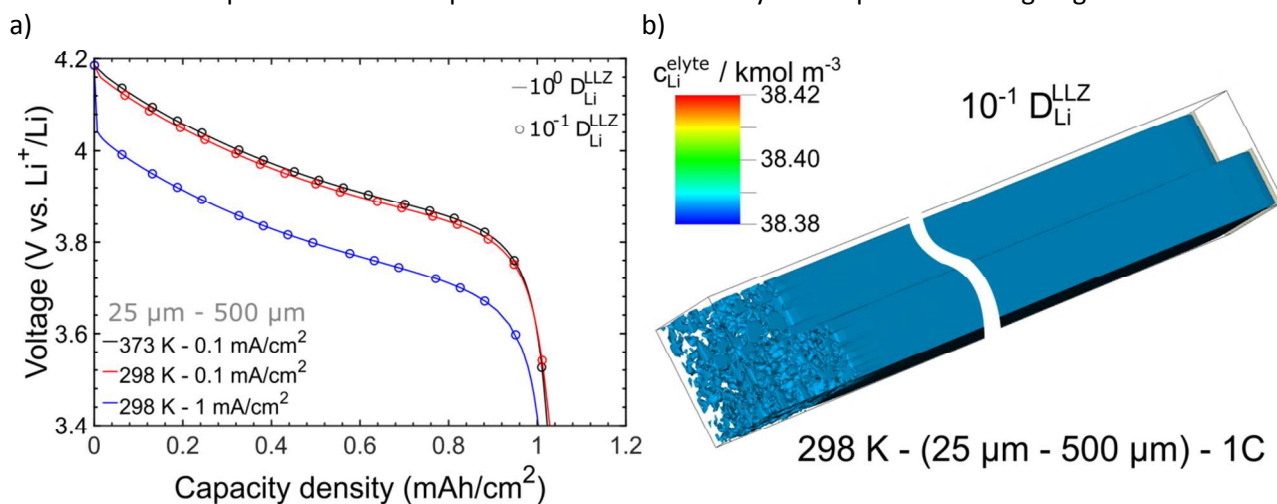


Figure S5 – Sensitivity of simulation results towards the estimated diffusion coefficient of Li in LLZ. a: Discharge curves. b: Concentration distribution of Li ions in the LLZ electrolyte at the end of a 1C lithiation process with low diffusion coefficient.

Conductivity of LLZ – Measurements of LLZ conductivity were performed using the LLZ electrolyte which was sintered at slightly higher temperatures for various operating temperatures. In the SEM images the pellet showed a quite homogeneous morphology. At the interface to the mixed cathode particles with bad contact could be identified in the micrographs. Therefore, we vary in our simulations the effective conductivity of the LLZ phase in the separator and mixed cathode. Results are presented in Figure S6 b. Up to a threshold of 5% of the original conductivity the loss in capacity was found to be moderate. However, above this threshold the cell voltage was found to drop almost instantly below the cut-off voltage. Such a drop in effective conductivity in the whole LLZ phase (separator + mixed cathode) is rather unlikely. However, locally such conditions might apply due to inhomogeneous sintering conditions etc. For instance, the mixed cathode was sintered at slightly lower temperatures compared to the LLZ pellet in order to avoid the formation of secondary phases. If the local temperature in the mixed cathode was not high enough to provide optimal sintering conditions grain boundaries in the electrolyte phase might decrease LLZ conductivity. Figure S6 b shows discharge curves for decreasing conductivities of the LLZ phase in the mixed cathode. Grain boundaries are expected to decrease the conductivity by 3-5 orders of magnitude. In our simulations we observed a decrease in capacity by roughly a factor of 2 for a five orders of magnitude loss in effective conductivity.

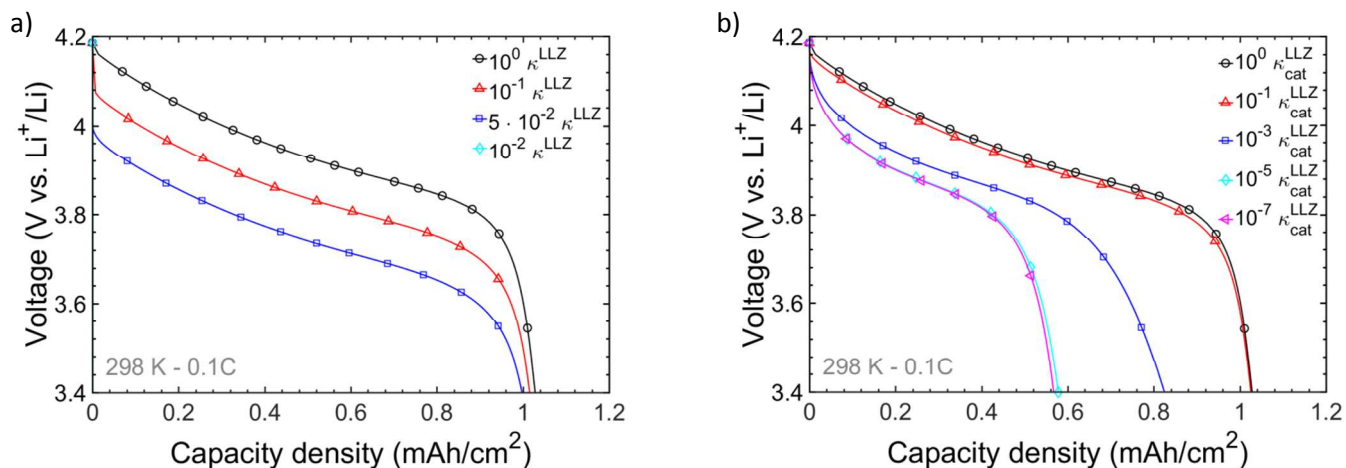


Figure S6 – Variation of LLZ conductivity for 0.1 C discharge simulations at room temperature. a: Variation of LLZ conductivity in the mixed cathode and separator pellet. b: Variation of LLZ conductivity in the mixed cathode only.

Diffusion of Li in LCO – A solid phase diffusion coefficient for Li of around 10^{-10} cm^2/s at room temperature is a typical value found for LCO in the literature ³. However, it was reported that the chemical diffusion coefficient depends on the crystal structure, orientation, and degree of lithiation of the material. Depending on the measurement technique values between 10^{-9} cm^2/s and 10^{-13} cm^2/s were reported ⁴⁻⁵. Starting with a standard value of 10^{-10} cm^2/s ($10^0 D_{Li}^{LCO}$) we investigate the influence of decreasing diffusion coefficient in Figure S7. Solid lines represent simulation results with diffusion coefficients going down to 10^{-15} cm^2/s ($10^{-5} D_{Li}^{LCO}$). The dashed lines are the same results but were shifted by the activation and transport overpotentials observed in the experimental data at room temperature. The simulations show a decrease in capacity for lower diffusion coefficients. However, even with a diffusion coefficient which is 5 orders of magnitude smaller, and thus much lower than the expected average value, we do not see the significant capacity loss which is observed experimentally. Figure S7 b shows the distribution of Li ions at the end of discharge (red-fully lithiated; blue – initial degree of lithiation). For small diffusion coefficients we see a lithiation of the surface layer only. Therefore, lower capacity can be expected in simulations with higher resolution. Such very low diffusion coefficients could be rationalized by surface layers of degraded material.

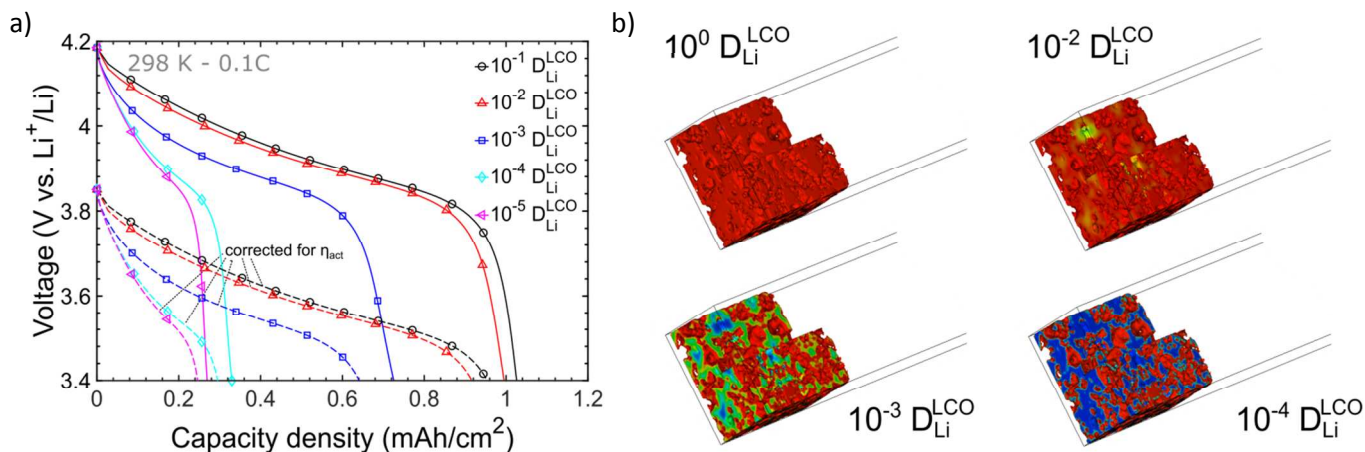


Figure S7 – Variation of the diffusion coefficient of Li in the LCO phase. Simulations were performed on a 25 μm as reconstructed geometry with a 500 μm separator at room temperature. **a:** Discharge curves with decreasing capacity towards smaller diffusion coefficients. **b:** Distribution of Li in LCO at the end of discharge. Red color indicates fully lithiated areas, blue color represents the initial degree of lithiation.

Conductivity of LCO – Similar to the diffusion coefficient also the electronic conductivity of LCO changes with both Li content and temperature. Significant activation energies are found only above $x=0.95$ in Li_xCoO_2 .⁶ Therefore, temperature dependence can be almost neglected. Including the strong decrease above $x=0.95$, the LCO electronic conductivity varies 4 orders of magnitude with Li content between $x=0.45$ and $x=1$ ranging from 10^1 to 10^{-3} S/cm, respectively. The simulation approach was used to evaluate the influence of a low conductivity on electrode performance. The results of the study are presented in Figure S8. The standard conductivity of LCO in this work is 1 S/cm and down to 10^{-3} S/cm practically no influence of LCO conductivity on cell performance could be found. This can be rationalized by comparing the electrical conductivity of LCO to the ionic conductivity of LLZ which is roughly 4 orders of magnitude larger at room temperature. As expected from this large difference, electron transport only becomes limiting at much lower values and has a neglectable effect even when on the same order of magnitude as the ionic conductivity in the LLZ phase (represented by the blue diamonds in Figure S8). The small effect is still illustrated in the insets shown in Figure S8. Evaluation of the potential distribution in the mixed cathode shows a maximum potential difference between different electrode regions of around 40 mV at low conductivity compared to less than 4 mV at higher conductivity.

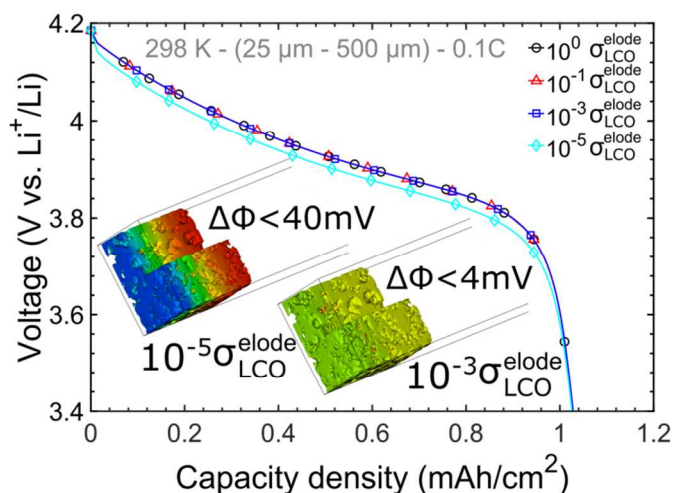


Figure S8 – Variation of LCO conductivity in a ‘as reconstructed’ cathode geometry of 25 μm thickness combined with a 500 μm separator. Discharge curves show a negligible influence of the LCO conductivity on cell performance down to 10⁻¹ S/m. Insets present the corresponding potential distribution at the end of discharge for $\sigma_{\text{LCO}}^{\text{elode}} = 10^{-1} \text{ S/m}$ and $\sigma_{\text{LCO}}^{\text{elode}} = 10^{-3} \text{ S/m}$, respectively.

Kinetic factors – One of the challenges in the development of new solid electrolytes is the stability of the different materials. In the literature numerous reports of parasitic degradation products at both cathode and anode can be found⁷⁻⁹. These degradation products have a negative effect on both transport and insertion kinetics. In this section we try to investigate the sensitivity of our simulations towards a change in the exchange current density factor, which can be seen as a first approximation but does not represent a comprehensive study. As standard value we use pre-exponential factors which were found to give good results for liquid electrolytes at room temperature. Figure S9 shows discharge curves for decreasing exchange current density factors at the mixed cathode (a) and Li foil (b). If one would ascribe the whole initial potential loss observed in the experiments (included as dashed line) to either anode or cathode one would get a decrease in the kinetic factors between 3 and 4 orders of magnitude. In the literature activation overpotentials of around 0.1 V at a current density of 0.1 mA/cm² were reported for a Li metal anode. Taking this into account the decrease in insertion kinetics at the cathode can be estimated to around 2-3 orders of magnitude (dark blue curve) but still cannot account for the large deviation of the simulation to the room temperature performance.

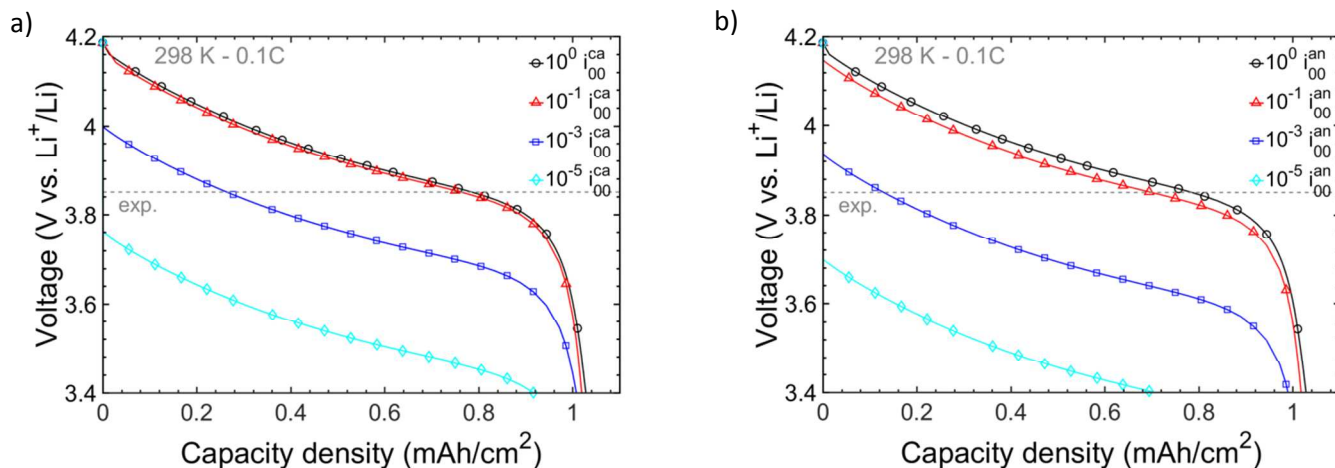


Figure S9 - Influence of exchange current density coefficients at the cathode (a) and anode (b) on cell voltage and battery performance. The dashed line gives the experimentally observed cell voltage at the beginning the discharge voltage for comparison.

Although we performed an extensive simulation study a final conclusion regarding the enormous loss in capacity at room temperature could not be found. However, in this study we did not include insulating surface layers of secondary phases, transport of Li through space charge layers in the LLZ electrolyte, or electromechanical effects which are known to be an issue. Expanding our model to include these effect on a fundamental level might finally resolve the discrepancy. Anyhow, the issue of dominating interface effects needs to be resolved for a successful commercialization of oxide based ASBs on a fundamental level using mechanistic understanding of the materials and processes.

2.4 Effect of electrode thickness and geometry

Additionally, in order to provide capacity and currents which are needed e.g. in electric vehicles it is also mandatory to manufacture thicker electrodes with thinner separators to improve the energy and power density. Therefore, additional results on our design studies are provided in this section, focusing on virtual electrodes with a high areal capacity and a 10 μm separator. To obtain values that can be achieved in optimized cells, we base our design study on a well-developed electrode/electrolyte interface which shows similar performance compared to liquid electrolytes. A detailed analysis of loss mechanisms in state-of-the-art batteries at room temperature was given in the previous paragraph.

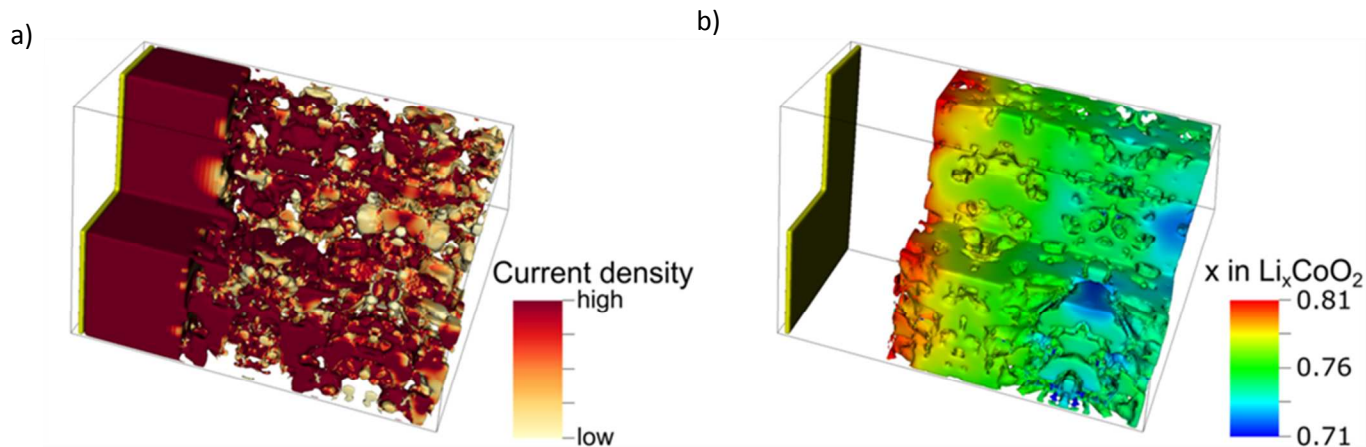


Figure S10 - a: Distribution of local current densities in the 10 μm LLZ electrolyte. b: corresponding Li concentration x in the Li_xCoO_2 of the 25 μm mixed cathode at 50% depth-of-discharge with 1 mA cm^{-2} (1C) at RT.

At moderate C-rates we did not observe significant transport limitations in our simulations. Figure S11 shows discharge curves of a battery with a 100 μm electrode at C/10 rate. The capacity is close to the theoretical capacity of the material and ohmic losses are marginal.

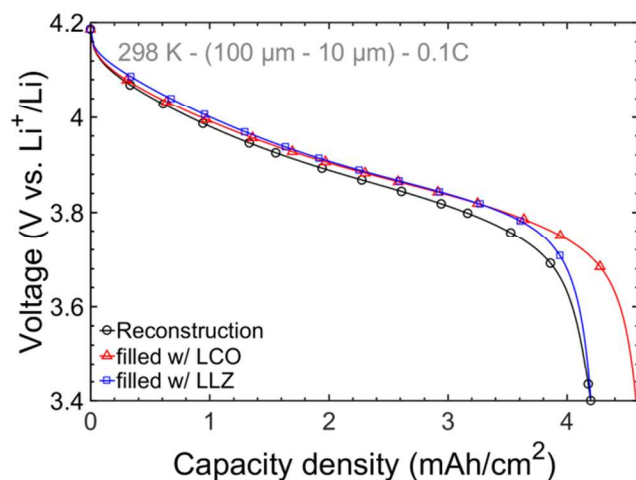


Figure S11 – Lithiation curves of the 100 μm mixed cathode with 0.1C rate. Different lines indicate the geometry cases.

At high C-rates mass transport limitations are obvious and on a per electrode volume basis the 100 μm electrode shows a significant loss in performance compared to the 50 μm and 25 μm electrodes. Corresponding discharge curves are shown in Figure S12. The images on the right hand side of Figure S12 show the distribution of lithium in LCO at the end of a 1C discharge. The thin electrodes are almost ideally utilized but the 100 μm electrode shows a gradient in Li distribution with fully lithiated particles close to the separator and particles at their initial concentration close to the cathode current collector. Consequently the volumetric capacity is only half of the smaller electrodes. This is indicative for transport limitations in the solid electrolyte and explains the gain in capacity for the filled w/ LLZ case and thus shows the need for compositional optimization depending on the final desired capacity density of the cell (high power vs. high energy density cells).

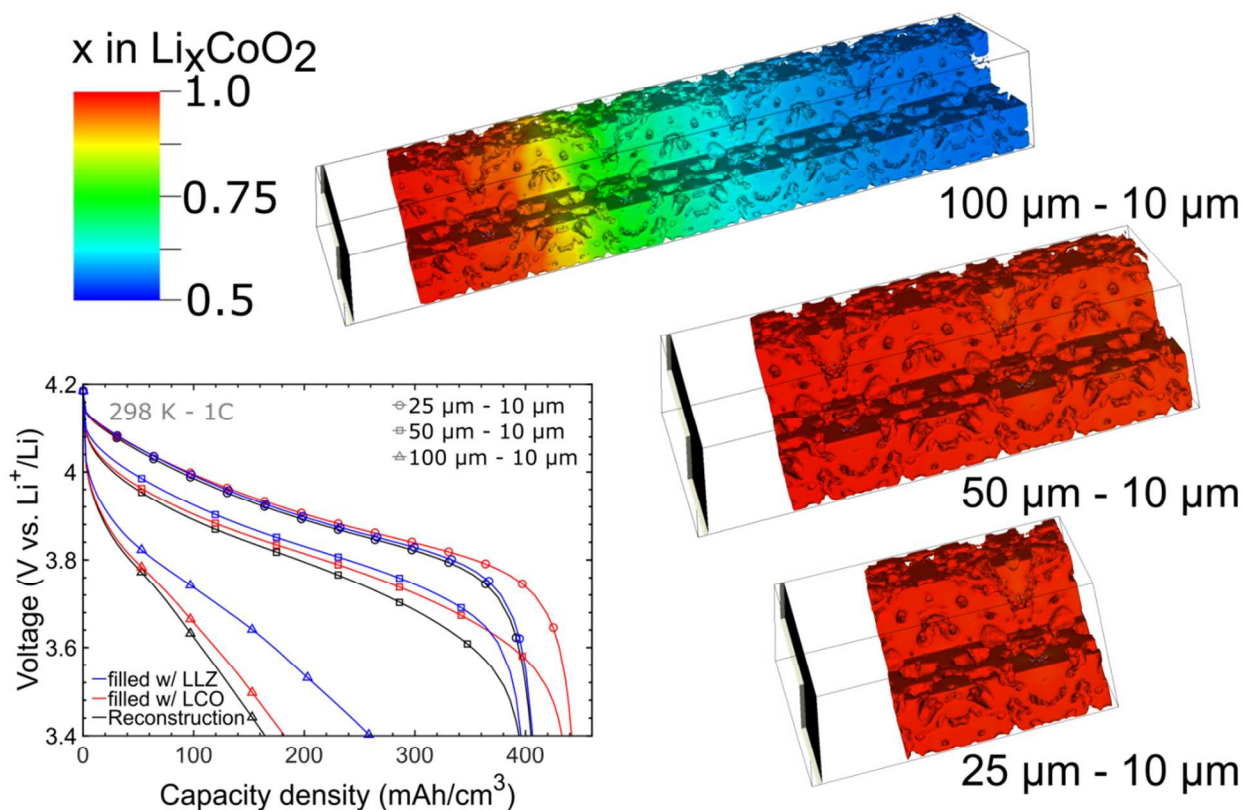


Figure S12 – Discharge curves as function of capacity per cathode volume for 25 μm , 50 μm , and 100 μm thick electrodes. The images present the corresponding distributions of Li in LCO for the as reconstructed electrode geometry at the lower cut-off voltage.

Figure S13 provides the potential and Li distributions in the electrolyte and active material at the end of a 1C discharge process. The images allow for a direct correlation between electrolyte transport and battery capacity for the cases ‘reconstruction’, ‘filled w/ LCO’, and ‘filled w/ LLZ’. Obviously, the transport limitations in the electrolyte indicated by a large gradient in potential cause a loss in capacity which can be seen in the local Li concentration at the end of discharge. Potential distributions in the as reconstructed geometry and filled w/ LCO case were found to be similar since the electrolyte network was not modified. Consequently, the practical capacity of the filled w/ LCO case improves only marginal. In contrary, optimization of the LLZ network, as in the filled w/ LLZ case, significantly improves ion transport and, therefore, capacity.

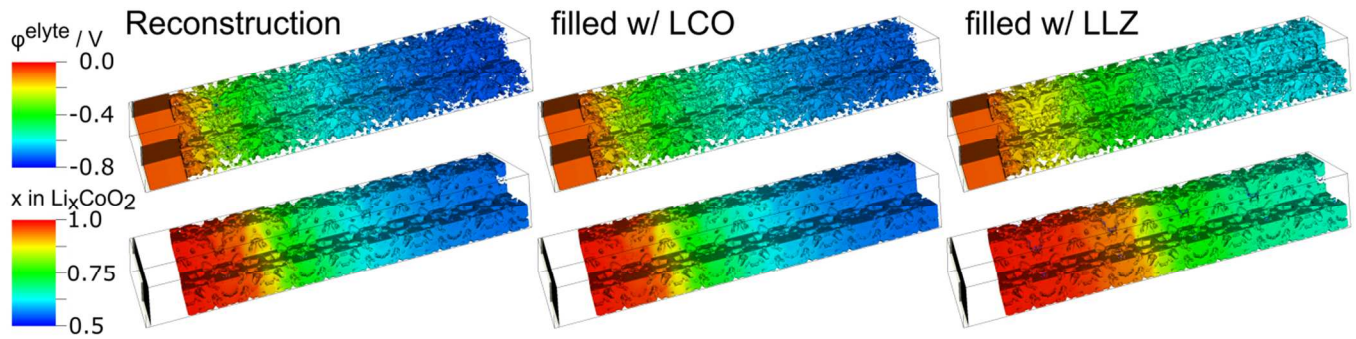


Figure S13 - Influence of electrode structure on battery performance for a discharge at 1C. Distribution of electrolyte potential and local Li concentration in the active material at the end of discharge.

Figure S14 shows the potential distribution in the solid electrolyte. At elevated conductivities corresponding to temperatures of 50 and 100°C, shown in Figure S15, the distribution is more homogeneous and thus ohmic losses less prominent. The faster transport of Li improves the utilization of the electrode and enables higher practical capacities.

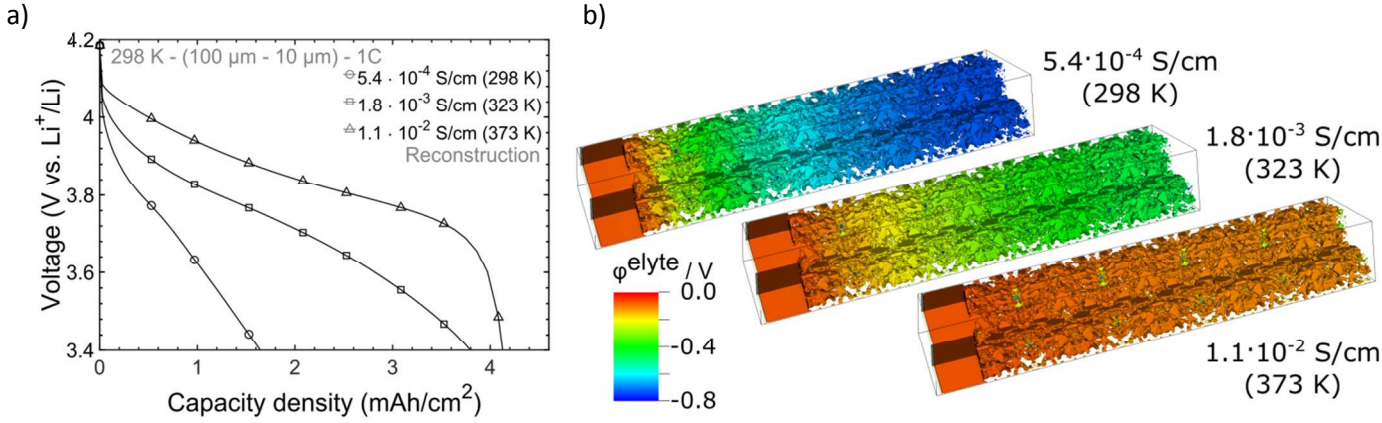


Figure S14 – Influence of LLZ conductivity on the performance of the mixed electrode. a) Lithiation curves. b) Distribution of electrolyte potential at the lower cut-off voltage.

In the case of the 25μm and 50μm electrodes transport losses were generally less prominent, as can be seen in Figure S15 – Influence of LLZ conductivity on battery performance for electrodes with a thickness of 25 μm (a) and 50 μm (b).Figure S15. Thus, the gain of an electrolyte with improved conductivity had no significant impact on the discharge capacity.

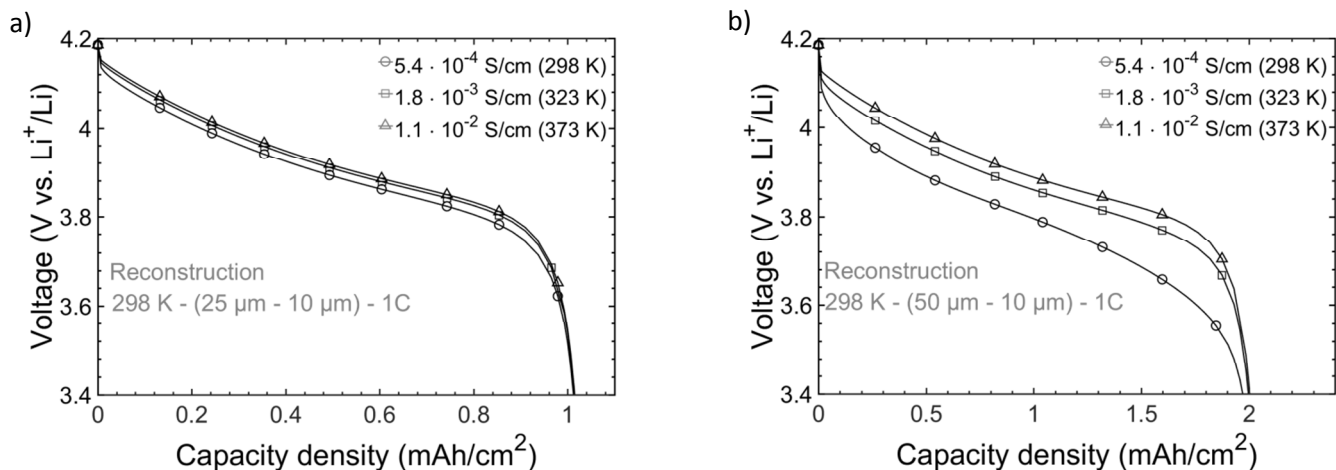


Figure S15 – Influence of LLZ conductivity on battery performance for electrodes with a thickness of 25 μm (a) and 50 μm (b).

In conclusion, supporting our statement in the main article, increasing the conductivity of the solid electrolyte might not be necessary or of lower priority if thin electrodes are used and a conductivity of at least 1×10^{-3} S/cm is needed to achieve reasonable capacity densities at room temperature.

References:

1. Sharafi, A.; Kazyak, E.; Davis, A. L.; Yu, S.; Thompson, T.; Siegel, D. J.; Dasgupta, N. P.; Sakamoto, J., Surface Chemistry Mechanism of Ultra-Low Interfacial Resistance in the Solid-State Electrolyte $\text{Li}_7\text{La}_3\text{Zr}_2\text{O}_{12}$. *Chemistry of Materials* **2017**, *29* (18), 7961-7968.
2. Ohser, J.; Mücklich, F., *Statistical Analysis of Microstructures in Materials Science*. Wiley and Sons: **2000**.
3. Ramadass, P.; Haran, B.; Gomadam, P. M.; White, R.; Popov, B. N., Development of First Principles Capacity Fade Model for Li-Ion Cells. *Journal of The Electrochemical Society* **2004**, *151*, A196.
4. Xia, H.; Lu, L.; Ceder, G., Li Diffusion in LiCoO_2 Thin Films Prepared by Pulsed Laser Deposition. *Journal of Power Sources* **2006**, *159* (2), 1422-1427.
5. Wang, B.; Bates, J. B.; Hart, F. X.; Sales, B. C.; Zuhr, R. A.; Robertson, J. D., Characterization of Thin-Film Rechargeable Lithium Batteries with Lithium Cobalt Oxide Cathodes. *Journal of the Electrochemical Society* **1996**, *143* (10), 3203-3213.
6. Molenda, J.; Stoklosa, A.; Bak, T., Modification in the Electronic-Structure of Cobalt Bronze Li_xCoO_2 and the Resulting Electrochemical Properties. *Solid State Ionics* **1989**, *36* (1-2), 53-58.
7. Miara, L.; Windmuller, A.; Tsai, C. L.; Richards, W. D.; Ma, Q. L.; Uhlenbruck, S.; Guillon, O.; Ceder, G., About the Compatibility between High Voltage Spinel Cathode Materials and Solid Oxide Electrolytes as a Function of Temperature. *ACS Appl Mater Inter* **2016**, *8* (40), 26842-26850.
8. Miara, L. J.; Richards, W. D.; Wang, Y. E.; Ceder, G., First-Principles Studies on Cation Dopants and Electrolyte Cathode Interphases for Lithium Garnets. *Chemistry of Materials* **2015**, *27* (11), 4040-4047.
9. Uhlenbruck, S.; Dornseiffer, J.; Lobe, S.; Dellen, C.; Tsai, C.-L.; Gotzen, B.; Sebold, D.; Finsterbusch, M.; Guillon, O., Cathode-Electrolyte Material Interactions During Manufacturing of Inorganic Solid-State Lithium Batteries. *Journal of Electroceramics* **2016**, 1-10.